Amplitude analysis and branching-fraction measurement of $D_s^+ \to \pi^+\pi^0\eta'$

The BESIII collaboration

E-mail: besiii-publications@ihep.ac.cn

ABSTRACT: Using data collected with the BESIII detector in e^+e^- collisions at center-of-mass energies between 4.178 and 4.226 GeV and corresponding to 6.32 fb^{-1} of integrated luminosity, we report the amplitude analysis and branching-fraction measurement of the $D_s^+ \to \pi^+\pi^0\eta'$ decay. We find that the dominant intermediate process is $D_s^+ \to \rho^+\eta'$ and the significances of other resonant and nonresonant processes are all less than 3σ. The upper limits on the branching fractions of S-wave and P-wave nonresonant components are set to 0.10% and 0.74% at the 90% confidence level, respectively. In addition, the branching fraction of the $D_s^+ \to \pi^+\pi^0\eta'$ decay is measured to be $(6.15 \pm 0.25(\text{stat.}) \pm 0.18(\text{syst.}))\%$, which receives significant contribution only from $D_s^+ \to \rho^+\eta'$ according to the amplitude analysis.

Contents

1 Introduction

Hadronic decays of the $D_s^{\pm}$ meson probe the interplay of short-distance weak-decay matrix elements and long distance QCD interactions. Measurements of the branching fractions (BFs) of these decays provide direct knowledge of the amplitudes and phases in the decay process [1–3]. In addition, an improved understanding of $D_s^{\pm}$ decays is particularly valuable for studies of the B_s^0 meson, which mainly decays to final states involving $D_s^{\pm}$ mesons [4].

There are two kinds of topological diagrams for $D_s^+ \to \rho^+ \eta'$, including tree (T)- and annihilation (A)-diagrams, as shown in figure 1 [5]. Based on reference [6], the topological amplitude ($\mathcal{A}$) expressions of $D_s^+ \to \rho^+\eta$, $D_s^+ \to \rho^+\eta'$ and $D_s^+ \to \pi^+\omega$ satisfy the sum rule:

$$\frac{1}{\sin\phi}\mathcal{A}(D_s^+ \to \pi^+\omega) = \frac{\cos\phi}{\sin\phi}\mathcal{A}(D_s^+ \to \rho^+\eta) + \mathcal{A}(D_s^+ \to \rho^+\eta'). \qquad (1.1)$$

Here, ϕ is the mixing angle between η and η':

$$\begin{pmatrix} \eta \\ \eta' \end{pmatrix} = \begin{pmatrix} \cos\phi & -\sin\phi \\ \sin\phi & \cos\phi \end{pmatrix} \begin{pmatrix} \eta_q \\ \eta_s \end{pmatrix}, \qquad (1.2)$$
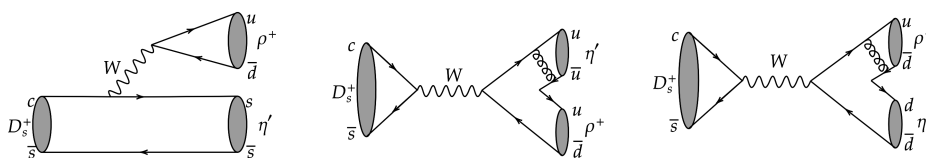
Figure 1. The T_P-diagram (left), A_V-diagram (middle) and A_P-diagram (right) for $D_s^+ \to \rho^+ \eta'$. The subscript $P(V)$ implies a pseudoscalar (vector) meson.
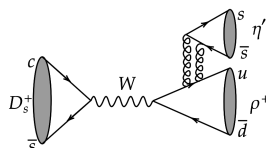

Figure 2. Hairpin-topological diagram for $D_s^+ \to \rho^+ \eta'$.

Decay		$\mathcal{B}(\%)$	
Theory	$D_s^+ \to \rho^+ \eta'$	3.0 ± 0.5 [7]	1.7 [8] 1.6 [8]
Experiment	$D_s^+ \to \pi^+ \pi^0 \eta'$	$5.6 \pm 0.5 \pm 0.6$	CLEO [9]
	$D_s^+ \to \rho^+ \eta'$	$5.8 \pm 1.4 \pm 0.4$	BESIII [10]
	$D_s^+ \to \pi^+ \pi^0 \eta'$	< 5.1	
	(nonresonant)	(90% confidence level)	

Table 1. $\mathcal{B}(D_s^+ \to \rho^+ \eta')$ from theoretical approaches and previous experimental measurements.

where η_q and η_s are defined by $\eta_q = \frac{1}{\sqrt{2}}(u\bar{u} + d\bar{d})$ and $\eta_s = s\bar{s}$. Considering the BFs of $D_s^+ \to \pi^+ \omega$ and $D_s^+ \to \rho^+ \eta$ and noting a simple triangular inequality in eq. (1.1), one obtains the bounds $(2.19 \pm 0.27)\% < \mathcal{B}(D_s^+ \to \rho^+ \eta') < (4.51 \pm 0.38)\%$ [6]. The predictions of the BF of $D_s^+ \to \rho^+ \eta'$ from several theoretical approaches [7, 8] and the corresponding BFs from experimental measurements are shown in table 1. The theoretical predictions for $\mathcal{B}(D_s^+ \to \rho^+ \eta')$ are lower than the experimental measurement by around 2σ as shown in table 1. A possible way to reconcile the predictions with the measured values would be to take account of the QCD flavor-singlet hairpin contribution shown in figure 2 [5]. A more precise measurement of the BF of $D_s^+ \to \rho^+ \eta'$ will be very valuable in establishing whether indeed the existing predictions are incorrect.

Previously, BESIII reported the BF measurement of $D_s^+ \to \rho^+ \eta'$ performed through the process $e^+ e^- \to D_s^+ D_s^-$, with a 482 pb^{-1} data sample collected at center-of-mass (C.M.) energy $\sqrt{s} = 4.009$ GeV and CLEO measured the BF of $D_s^+ \to \pi^+ \pi^0 \eta'$ using 586 pb^{-1} of $e^+ e^-$ collisions recorded at C.M. energy $\sqrt{s} = 4.17$ GeV. In this paper, we perform the first amplitude analysis of $D_s^+ \to \pi^+ \pi^0 \eta'$ and improve the BF measurement of this decay via the process $e^+ e^- \to D_s^{*\pm} D_s^{\mp}$ by using data samples corresponding to an integrated luminosity of 6.32 fb^{-1} collected by the BESIII detector at C.M. energies $\sqrt{s} = 4.178$–4.226 GeV. Charge-conjugate states are implied throughout this paper.

$\sqrt{s}$ (GeV)	$\mathcal{L}_{\text{int}}$ (pb^{-1})	M_{rec} (GeV/c^2)
4.178	3189.0±0.2±31.9	[2.050, 2.180]
4.189	526.7±0.1±2.2	[2.048, 2.190]
4.199	526.0±0.1±2.1	[2.046, 2.200]
4.209	517.1±0.1±1.8	[2.044, 2.210]
4.219	514.6±0.1±1.8	[2.042, 2.220]
4.226	1056.4±0.1±7.0	[2.040, 2.220]

Table 2. The integrated luminosities ($\mathcal{L}_{\text{int}}$) and the requirements on M_{rec} for various C.M. energies. The definition of M_{rec} is given in eq. (3.1). The first and second uncertainties are statistical and systematic, respectively.

2 Detector and data sets

The BESIII detector [11] records symmetric e^+e^- collisions provided by the BEPCII storage ring [12], which operates in the C.M. energy range from 2.00 to 4.95 GeV. BESIII has collected large data samples in this energy region [13]. The cylindrical core of the BESIII detector covers 93% of the full solid angle and consists of a helium-based multilayer drift chamber (MDC), a plastic scintillator time-of-flight system (TOF), and a CsI(Tl) electromagnetic calorimeter (EMC), which are all enclosed in a superconducting solenoidal magnet providing a 1.0 T magnetic field. The solenoid is supported by an octagonal flux-return yoke with resistive plate counter muon identification modules interleaved with steel. The charged-particle momentum resolution at 1 GeV/c is 0.5%, and the specific energy loss (dE/dx) resolution is 6% for electrons from Bhabha scattering. The EMC measures photon energies with a resolution of 2.5% (5%) at 1 GeV in the barrel (end-cap) region. The time resolution in the TOF barrel region is 68 ps, while that in the end-cap region is 110 ps. The end-cap TOF system was upgraded in 2015 using multi-gap resistive plate chamber technology, providing a time resolution of 60 ps [14–16].

The data samples used in this analysis are listed in table 2 [17]. Since the cross section of $D_s^{*\pm}D_s^{\mp}$ production in e^+e^- annihilation is about a factor of twenty larger than that of $D_s^+D_s^-$ [18] at C.M. energies $\sqrt{s} = 4.178$–4.226 GeV, and the $D_s^{*\pm}$ meson decays to $\gamma D_s^\pm$ with a dominant BF of $(93.5 \pm 0.7)\%$ [4], the signal events discussed in this paper are selected from the process $e^+e^- \to D_s^{*\pm}D_s^{\mp} \to \gamma D_s^+D_s^-$.

Simulated data samples produced with a GEANT4-based [19] Monte Carlo (MC) package, which includes the geometric description of the BESIII detector and the detector response, are used to determine detection efficiencies and to estimate backgrounds. The simulation models the beam energy spread and initial-state radiation (ISR) in the e^+e^- annihilations with the generator KKMC [20, 21]. The inclusive MC sample includes the production of open-charm processes, the ISR production of vector charmonium(-like) states, and the continuum processes incorporated in KKMC. The known decay modes are modelled with EVTGEN [22, 23] using BFs taken from the Particle Data Group (PDG) [4], and the re-

Tag mode	Mass window (GeV/c^2)
$D_s^- \to K_S^0 K^-$	[1.948, 1.991]
$D_s^- \to K^+ K^- \pi^-$	[1.950, 1.986]
$D_s^- \to K_S^0 K^- \pi^0$	[1.946, 1.987]
$D_s^- \to K_S^0 K^- \pi^- \pi^+$	[1.958, 1.980]
$D_s^- \to K_S^0 K^+ \pi^- \pi^-$	[1.953, 1.983]
$D_s^- \to \pi^- \eta_{\gamma\gamma}$	[1.930, 2.000]
$D_s^- \to \pi^- \eta'_{\pi^+\pi^-\eta_{\gamma\gamma}}$	[1.940, 1.996]
$D_s^- \to K^- \pi^+ \pi^-$	[1.953, 1.986]
$D_s^- \to K^- K^+ \pi^- \pi^0$	[1.947, 1.982]
$D_s^- \to \pi^- \pi^- \pi^+$	[1.952, 1.982]
$D_s^- \to \pi^- \eta_{\pi^+\pi^-\pi^0}$	[1.941, 1.990]
$D_s^- \to \pi^- \eta'_{\gamma\rho^0}$	[1.939, 1.992]

Table 3. Requirements on the tagging D_s^- mass (M_{tag}) for various tag modes, where the η and η' subscripts denote the decay modes used to reconstruct these particles.

maining unknown charmonium decays are modeled with LUNDCHARM [24–28]. Final-state radiation (FSR) from charged final state particles is incorporated using PHOTOS [29].

3 Event selection

The data samples were collected just above the $D_s^{*\pm} D_s^{\mp}$ threshold. The tag method [30] allows clean signal samples to be selected, providing an opportunity to perform amplitude analyses and to measure the absolute BFs of the hadronic D_s^+ meson decays. In the tag method, a single-tag (ST) candidate requires only one of the $D_s^{\pm}$ mesons to be reconstructed via a hadronic decay; a double-tag (DT) candidate has both $D_s^+ D_s^-$ mesons reconstructed via hadronic decays. The DT candidates are required to have the D_s^+ meson decaying to the signal mode $D_s^+ \to \pi^+ \pi^0 \eta'$ and the D_s^- meson decaying to twelve tag modes listed in table 3.

Charged tracks detected in the MDC are required to be within a polar angle (θ) range of $|\cos\theta| < 0.93$, where θ is defined with respect to the z-axis which is the symmetry axis of the MDC. For charged tracks not originating from K_S^0 decays, the distance of closest approach to the interaction point is required to be less than 10 cm along the beam direction and less than 1 cm in the plane perpendicular to the beam. Particle identification (PID) for charged tracks combines measurements of the dE/dx in the MDC and the flight time in the TOF to form a probability $\mathcal{L}(h)$ ($h = p, K, \pi$) for each hadron h hypothesis. Charged kaons and pions are identified by comparing the probability for the two hypotheses, $\mathcal{L}(K) > \mathcal{L}(\pi)$ and $\mathcal{L}(\pi) > \mathcal{L}(K)$, respectively.

The K_S^0 candidates are selected by looping over all pairs of tracks with opposite charges, whose distances to the interaction point along the beam direction are within 20 cm. These two tracks are assumed to be pions without PID applied. A primary vertex and a secondary vertex are reconstructed and the decay length between the two vertexes is required to be greater than twice its uncertainty. This requirement is not applied for the $D_s^- \to K_S^0 K^-$ decay due to the low combinatorial background. Candidate K_S^0 particles are required to have the vertex fit and an invariant mass of the $\pi^+\pi^-$ pair ($M_{\pi^+\pi^-}$) in the range [0.487, 0.511] GeV/c^2. To prevent an event being doubly counted in the $D_s^- \to K_S^0 K^-$ and $D_s^- \to K^-\pi^+\pi^-$ selections, the value of $M_{\pi^+\pi^-}$ is required to be outside of the mass range [0.487, 0.511] GeV/c^2 for $D_s^- \to K^-\pi^+\pi^-$ decay.

Photon candidates are identified using showers in the EMC. The deposited energy of each shower must be more than 25 MeV in the barrel region ($|\cos\theta| < 0.80$) and more than 50 MeV in the end cap region ($0.86 < |\cos\theta| < 0.92$). The opening angle between the position of each shower in the EMC and the closest extrapolated charged track must be greater than 10 degrees to exclude showers that originate from charged tracks. The difference between the EMC time and the event start time is required to be within [0, 700] ns to suppress electronic noise and showers unrelated to the event.

The π^0 (η) candidates are reconstructed through $\pi^0 \to \gamma\gamma$ ($\eta \to \gamma\gamma$) decays, with at least one photon falling in the barrel region. The invariant mass of the photon pair for π^0 and η candidates must be in the ranges $[0.115, 0.150]$ GeV/c^2 and $[0.500, 0.570]$ GeV/c^2, respectively, which are about three times larger than the detector resolution. A kinematic fit that constrains the $\gamma\gamma$ invariant mass to the π^0 or η known mass [4] is performed to improve the mass resolution. The η candidates are also reconstructed through $\eta \to \pi^+\pi^-\pi^0$ and the invariant mass of $\pi^+\pi^-\pi^0$ are required to satisfy the range of $[0.530, 0.560]$ GeV/c^2. The ρ^0 candidates are selected via the decay $\rho^0 \to \pi^+\pi^-$ with an invariant mass window $[0.620, 0.920]$ GeV/c^2. The η' candidates are formed from the $\pi^+\pi^-\eta$ and $\gamma\rho^0$ combinations with an invariant mass within a range of $[0.946, 0.970]$ GeV/c^2.

Twelve tag modes are reconstructed and the corresponding mass windows on the tagging D_s^- mass ($M_{\rm tag}$) are listed in table 3. The $D_s^\pm$ candidates with $M_{\rm rec}$ lying within the mass windows listed in table 2 are retained for further study. The quantity $M_{\rm rec}$ is the recoil mass of $D_s^\pm$ and is defined as

$$M_{\rm rec} = \sqrt{\left(E_{\rm cm} - \sqrt{|\vec{p}_{D_s}|^2 + m_{D_s}^2}\right)^2 - |\vec{p}_{D_s}|^2}\,, \tag{3.1}$$

where $E_{\rm cm}$ is the initial energy of the e^+e^- C.M. system, $\vec{p}_{D_s}$ is the three-momentum of the $D_s^\pm$ candidate in the e^+e^- C.M. frame, and m_{D_s} is the $D_s^\pm$ known mass [4].

4 Amplitude analysis

4.1 Further event selection

The ST D_s^- mesons are reconstructed using the first eight hadronic decays as shown in table 3 and the following selection criteria are further applied in order to obtain data samples with high purities for the amplitude analysis. The selection criteria discussed in

this section are not used in the BF measurement since the BF measurement is dominated by statistical uncertainty.

After a tag D_s^- is identified, the signal candidate is selected by requiring one η' candidate, one track identified as a charged pion and one π^0 candidate, where π^0 and η' candidates are selected by the same requirements described in section 3, but include the decay $\eta' \to \pi^+\pi^-\eta$; $\eta \to \gamma\gamma$ only. Then, an nine-constraint (9C) kinematic fit is performed to the process $e^+e^- \to D_s^{*\pm}D_s^\mp \to \gamma D_s^+ D_s^-$ assuming the D_s^- decays to one of the tag modes and the D_s^+ decays to the signal mode. Two hypotheses are considered: that the signal D_s^+ comes from a D_s^{*+} meson or the tag D_s^- comes from a D_s^{*-} meson. The invariant masses of $(\gamma\gamma)_{\pi^0}$, $(\gamma\gamma)_\eta$, $(\pi^+\pi^0\eta)_{\eta'}$, tag D_s^-, and $D_s^{*\pm}$ candidates are constrained to the corresponding known masses [4] and the constraints of four-momentum conservation in the e^+e^- C.M. system are also applied. The $D_s^{*\pm}D_s^\mp$ combination with the minimum χ^2_{9C} is chosen. In order to ensure that all candidates fall within the phase-space boundary, the constraint of the signal D_s^+ mass is added to the 9C kinematic fit and the updated four-momenta are used for the amplitude analysis.

To suppress background from fake η candidates, we check the invariant-mass distributions of the $\gamma\gamma$ combination ($M_{\text{recombined}}$) which can be with one photon from the signal η (η_{sig}) and the other photon from the signal π^0, D_s^* or the η/π^0 on the tag side. Events with $|M_{\text{recombined}} - M_{\pi^0}| < 0.015\,\text{GeV}/c^2$ and $|M_{\text{recombined}} - M_{\pi^0}| < |M_{\eta_{\text{sig}}} - M_\eta|$ are rejected, where $M_{\eta_{\text{sig}}}$ is the invariant mass of the photon pair for η_{sig} candidates, while M_{π^0} and M_η are the π^0 and η known masses [4], respectively.

Figure 3 shows the fits to the invariant-mass distributions of the accepted signal D_s^+ candidates, M_{sig}, for the data samples at $\sqrt{s} =$4.178–4.226 GeV. The signal is described by a MC-simulated shape convolved with a Gaussian resolution function, and the background is described by a linear function. Finally, a mass window, $[1.92, 2.00]\,\text{GeV}/c^2$, is applied on the signal D_s^+ candidates. A total of 411 events are retained for the amplitude analysis with a purity, w_{sig}, of $(96.1 \pm 0.9)\%$.

4.2 Fit method

The composition of intermediate resonances in the decay $D_s^+ \to \pi^+\pi^0\eta'$ is determined by an unbinned maximum-likelihood fit to data. The likelihood function is constructed with a probability density function (PDF), which depends on the momenta of the three daughter particles. The amplitude of the nth intermediate state ($\mathcal{A}_n$) is given by

$$\mathcal{A}_n = P_n S_n F_n^r F_n^{D_s}, \tag{4.1}$$

where S_n and $F_n^{r(D_s)}$ are the spin factor and the Blatt-Weisskopf barriers of the intermediate state (the $D_s^\pm$ meson), respectively, and P_n is the propagator of the intermediate resonance.

The nonresonant amplitudes $\mathcal{N}_L$ where L denotes the orbital angular momentum between the $\pi^+\pi^0$ system with $L = 0$ (S wave), 1 (P wave), 2 (D wave) are similar to $\mathcal{A}_n$ in eq. (4.1) but do not contain resonant propagator terms P_n:

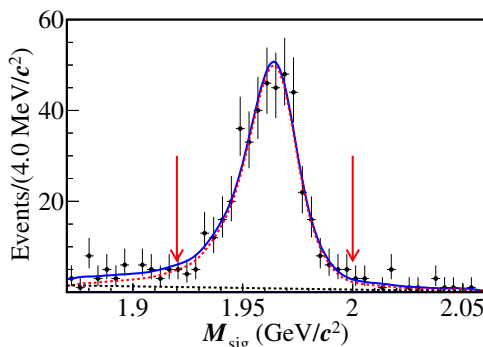$$\mathcal{N}_L = S_n F_n^r F_n^{D_s}, \tag{4.2}$$

Figure 3. Fit to the M_{sig} distribution of the data samples at $\sqrt{s} = 4.178$–$4.226\,\text{GeV}$. This plot is obtained using first eight tag modes in table 3. The black points with error bars are data. The blue line is the total fit. The red and black dashed lines are the fitted signal and background, respectively. The pair of red arrows indicate the selected signal region.

The total amplitude $\mathcal{M}$ is then the coherent sum of the amplitudes of intermediate processes, $\mathcal{M} = \sum \rho_n e^{i\phi_n} \mathcal{A}_n + \sum \rho_L e^{i\phi_L} \mathcal{N}_L$, where the parameters ρ_n and ϕ_n are the magnitudes and phases of the nth resonance, while ρ_L and ϕ_L correspond to the magnitudes and phases of the nonresonant contribution with angular momentum L.

The signal PDF $f_S(p_j)$ is written as

$$f_S(p_j) = \frac{\epsilon(p_j)\,|\mathcal{M}(p_j)|^2\,R_3(p_j)}{\int \epsilon(p_j)\,|\mathcal{M}(p_j)|^2\,R_3(p_j)\,dp_j}\,, \tag{4.3}$$

where $\epsilon(p_j)$ is the detection efficiency parameterized in terms of the final four-momenta p_j. The index j refers to the different particles in the final states, and $R_3(p_j)$ is the standard element of three-body phase space. The normalization integral is determined by a MC integration,

$$\int \epsilon(p_j)\,|\mathcal{M}(p_j)|^2\,R_3(p_j)\,dp_j \approx \frac{1}{N_{\text{MC}}} \sum_k^{N_{\text{MC}}} \frac{\left|\mathcal{M}(p_j^k)\right|^2}{\left|\mathcal{M}^g(p_j^k)\right|^2}\,, \tag{4.4}$$

where k is the index of the kth event and N_{MC} is the number of the selected MC events. Here $\mathcal{M}^g(p_j)$ is the PDF used to generate the MC samples in MC integration. To account for any bias caused by differences in tracking and PID efficiencies, and π^0 and η reconstruction efficiencies between data and MC simulation, each MC event is weighted with a ratio, $\gamma_\epsilon(p)$, between the efficiency of data and MC simulation. Then the MC integral becomes

$$\int \epsilon(p_j)\,|\mathcal{M}(p_j)|^2\,R_3(p_j)\,dp_j \approx \frac{1}{N_{\text{MC}}} \sum_k^{N_{\text{MC}}} \frac{\left|\mathcal{M}(p_j^k)\right|^2 \gamma_\epsilon(p_j^k)}{\left|\mathcal{M}^g(p_j^k)\right|^2}\,. \tag{4.5}$$

A signal-background combined PDF is introduced to account for the background in this analysis. The background PDF is given by

$$f_B(p_j) = \frac{B(p_j)R_3(p_j)}{\int B(p_j)R_3(p_j)\,dp_j}\,. \tag{4.6}$$

The background events in the signal region from the inclusive MC sample are used to model the corresponding background in data. This background description is validated by comparing the $M_{\pi^+\eta'}$, $M_{\pi^+\pi^0}$ and $M_{\pi^0\eta'}$ distributions of events outside the M_{sig} signal region between the data and the inclusive MC samples. The distributions of background events from the inclusive MC sample within and outside the M_{sig} signal region are also examined. They are found to be compatible within statistical uncertainties. The background shape $B(p_j)$ is a probability density function sampled from a multidimensional histogram by using RooHistPdf implemented in RooFit [31]. This background PDF is then added to the signal PDF incoherently and the combined PDF is written as

$$
\begin{aligned}
&w_{\text{sig}} f_S(p_j) + (1 - w_{\text{sig}}) f_B(p_j) \\
&= w_{\text{sig}} \frac{\epsilon(p_j) \left|\mathcal{M}(p_j)\right|^2 R_3(p_j)}{\int \epsilon(p_j) \left|\mathcal{M}(p_j)\right|^2 R_3(p_j)\, dp_j} + (1 - w_{\text{sig}}) \frac{B(p_j) R_3(p_j)}{\int B(p_j) R_3(p_j)\, dp_j}\,.
\end{aligned}
\tag{4.7}
$$

A efficiency-corrected background shape, $B_\epsilon(p_j) \equiv B(p_j)/\epsilon(p_j)$ is introduced in order to factorize the $\epsilon(p_j)$ term out from the combined PDF. In this way, the $\epsilon(p_j)$ term, which is independent of the fitted variables, is regarded as a constant and can be dropped during the log-likelihood fit. As a consequence, the combined PDF becomes

$$
\begin{aligned}
&w_{\text{sig}} f_S(p_j) + (1 - w_{\text{sig}}) f_B(p_j) \\
&= \epsilon(p_j) R_3(p_j) \left[\frac{w_{\text{sig}} \left|\mathcal{M}(p_j)\right|^2}{\int \epsilon(p_j) \left|\mathcal{M}(p_j)\right|^2 R_3(p_j)\, dp_j} + \frac{(1 - w_{\text{sig}}) B_\epsilon(p_j)}{\int \epsilon(p_j) B_\epsilon(p_j) R_3(p_j)\, dp_j} \right]\,.
\end{aligned}
\tag{4.8}
$$

Next, the integration in the denominator of the background term can also be handled by the MC integration method in the same way as for the signal only sample:

$$
\int \epsilon(p_j) B_\epsilon(p_j) R_3(p_j)\, dp_j \approx \frac{1}{N_{\text{MC}}} \sum_k^{N_{\text{MC}}} \frac{B_\epsilon(p_j^k)}{\left|\mathcal{M}^g(p_j^k)\right|^2}\,.
\tag{4.9}
$$

The final log-likelihood function is written as

$$
\ln \mathcal{L} = \sum_k^{N_D} \ln \left[w_{\text{sig}} f_S(p_j^k) + (1 - w_{\text{sig}}) f_B(p_j^k) \right]\,,
\tag{4.10}
$$

where N_D is the number of candidate events in data.

4.2.1 Blatt-Weisskopf barrier factors

For the process $a \to bc$, the Blatt-Weisskopf barrier $F_L(p_j)$ [32] is parameterized as a function of the angular momenta L and the momenta q of the daughter b or c in the rest system of a,

$$
\begin{aligned}
F_{L=0}(q) &= 1, \\
F_{L=1}(q) &= \sqrt{\frac{z_0^2 + 1}{z^2 + 1}}, \\
F_{L=2}(q) &= \sqrt{\frac{z_0^4 + 3z_0^2 + 9}{z^4 + 3z^2 + 9}},
\end{aligned}
\tag{4.11}
$$

where $z = qR$ and $z_0 = q_0 R$. Here q_0 represents the values of q, when the invariant mass is equal to the nominal mass of the resonance. The effective radius of the barrier R is fixed to $3.0\,\mathrm{GeV}^{-1}$ for the intermediate resonances and $5.0\,\mathrm{GeV}^{-1}$ for the D_s^+ meson.

4.2.2 Propagator

The intermediate resonances $a_0(1450)$, $a_2(1320)$, $\pi_1(1400)$ and $\pi_1(1600)$ are parameterized as relativistic Breit-Wigner functions,

$$
P = \frac{1}{m_0^2 - s_a - im_0\Gamma(m)}\,,
$$
$$
\Gamma(m) = \Gamma_0 \left(\frac{q}{q_0}\right)^{2L+1} \left(\frac{m_0}{m}\right) \left(\frac{F_L(q)}{F_L(q_0)}\right)^2 ,
$$
(4.12)

where s_a denotes the invariant-mass squared of the parent particle; m_0 and Γ_0 are the nominal mass and width of each intermediate resonance, respectively.

We parameterize the ρ^0 resonance by the Gounaris-Sakurai lineshape [33], which is given by

$$
P_{\mathrm{GS}}(m) = \frac{1 + d\frac{\Gamma_0}{m_0}}{m_0^2 - m^2 + f(m) - im_0\Gamma(m)}\,,
$$
(4.13)

where

$$
d = \frac{3m_\pi^2}{\pi q_0^2} \ln\left(\frac{m_0 + 2q_0}{2m_\pi}\right) + \frac{m_0}{2\pi q_0} - \frac{m_\pi^2 m_0}{\pi q_0^3}\,.
$$
(4.14)

The function $f(m)$ is given by

$$
f(m) = \Gamma_0 \frac{m_0^2}{q_0^3} \left[q^2(h(m) - h(m_0)) + (m_0^2 - m^2)q_0^2 \left.\frac{dh}{d(m^2)}\right|_{m_0^2}\right]\,,
$$
(4.15)

where

$$
h(m) = \frac{2q}{\pi m} \ln\left(\frac{m + 2q}{2m_\pi}\right)
$$
(4.16)

and

$$
\left.\frac{dh}{d(m^2)}\right|_{m_0^2} = h(m_0)\left[(8q_0^2)^{-1} - (2m_0^2)^{-1}\right] + (2\pi m_0^2)^{-1}\,.
$$
(4.17)

4.2.3 Spin factors

The spin-projection operators are defined as [34]

$$
P_{\mu\mu'}^{(1)}(a) = -g_{\mu\mu'} + \frac{p_{a,\mu}p_{a,\mu'}}{p_a^2}\,,
$$
$$
P_{\mu\nu\mu'\nu'}^{(2)}(a) = \frac{1}{2}(P_{\mu\mu'}^{(1)}(a)P_{\nu\nu'}^{(1)}(a) + P_{\mu\nu'}^{(1)}(a)P_{\nu\mu'}^{(1)}(a))
$$
$$
- \frac{1}{3}P_{\mu\nu}^{(1)}(a)P_{\mu'\nu'}^{(1)}(a)\,.
$$
(4.18)

The quantities p_a, p_b, and p_c are the momenta of particles a, b, and c, respectively, and $r_a = p_b - p_c$. The covariant tensors are given by

$$
\tilde{t}_\mu^{(1)}(a) = -P_{\mu\mu'}^{(1)}(a)r_a^{\mu'}\,,
$$
$$
\tilde{t}_{\mu\nu}^{(2)}(a) = P_{\mu\nu\mu'\nu'}^{(2)}(a)r_a^{\mu'}r_a^{\nu'}\,.
$$
(4.19)

The spin factors for S, P, and D wave decays are

$$\begin{aligned}
S &= 1\,, & &(S\ \text{wave}),\\
S &= \tilde{T}^{(1)\mu}(D_s^{\pm})\tilde{t}^{(1)}_{\mu}(a)\,, & &(P\ \text{wave}),\\
S &= \tilde{T}^{(2)\mu\nu}(D_s^{\pm})\tilde{t}^{(2)}_{\mu\nu}(a)\,, & &(D\ \text{wave}),
\end{aligned} \qquad (4.20)$$

where the $\tilde{T}^{(l)}$ factors have the same definitions as $\tilde{t}^{(l)}$. The tensor describing the D_s^+ decay is denoted by $\tilde{T}$ and that of the a decay is denoted by $\tilde{t}$.

4.3 Fit results

The Dalitz plots of $M^2_{\pi^+\pi^0}$ versus $M^2_{\eta'\pi^+}$ for the data samples and the signal MC samples generated based on the results of the amplitude analysis are shown in figure 4(a) and figure 4(b), respectively. One can see a clear ρ^+ resonance. Therefore we choose the $D_s^+ \to \rho^+\eta'$ amplitude as a reference, and fix the magnitude and the phase of its amplitude to 1.0 and 0.0, respectively, while those of other amplitudes are floated. The masses and widths of all resonances are fixed to the corresponding PDG averages [4], and w_{sig} are fixed to the purities discussed in section 4.1. Then we test other possible intermediate resonances, such as $\rho(1450)$, $a_0(1450)$, $\pi_1(1600)$, $a_2(1320)$, etc., by adding them one by one. We also examined the possible combinations of these intermediate resonances to check their significances, correlations and interferences. We use the difference of log-likelihoods of fits with and without these amplitudes to calculate the significance and find that in all cases these significances are less than three standard deviations. The significance of each intermediate resonance tested is listed in table 4. Hence the final model consists only of the mode $D_s^+ \to \rho^+\eta'$. The mass projections of the fit results are shown in figure 5.

In addition, we also try including the S-wave and P-wave nonresonant components, which are denoted as $D_s^+ \to (\pi^+\pi^0)_S\eta'$ and $D_s^+ \to (\pi^+\pi^0)_P\eta'$, respectively. The significances of the nonresonant processes are both less than three standard deviations. For the BFs of nonresonant decays, we scan the magnitudes of the nonresonant decays to obtain the likelihood variation versus the expected BF as shown in figure 6. To take the uncertainty of total BF shown in table 9 and systematic uncertainty of amplitude analysis listed in table 5 into account, the likelihood is convolved with a Gaussian function with a width equal to the total systematic uncertainty. The total systematic uncertainties of S-wave and P-wave components are 2.9% and 4.4%, respectively. Finally, we obtain the upper limits $\mathcal{B}(D_s^+ \to (\pi^+\pi^0)_S\eta') < 0.10\%$ and $\mathcal{B}(D_s^+ \to (\pi^+\pi^0)_P\eta') < 0.74\%$ at the 90% confidence level.

4.4 Systematic uncertainties for amplitude analysis

The following four sources of potential bias are considered when assigning systematic uncertainties.

i Resonance parameters. The uncertainties related to the fixed parameters in the amplitudes are estimated by varying the masse and width of the ρ^+ resonance by $\pm 1\sigma$ [4].
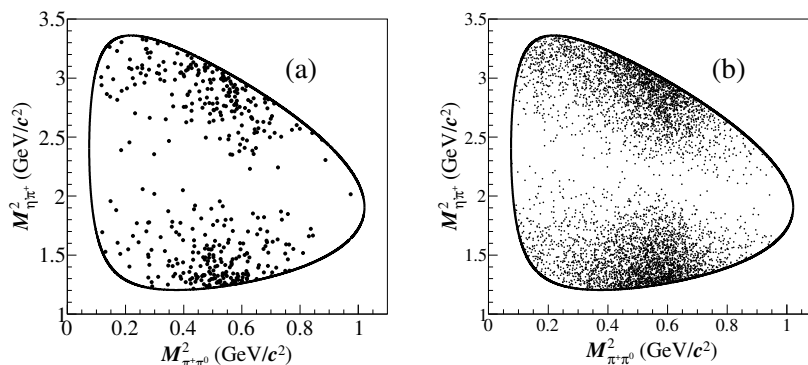
Figure 4. The Dalitz plots of $m^2_{\eta'\pi^+}$ versus $m^2_{\pi^+\pi^0}$ for (a) the data sample and (b) the signal MC samples generated based on the results of the amplitude analysis at $\sqrt{s} = 4.178 - 4.226\,\mathrm{GeV}$. The physical border is indicated by the black line.
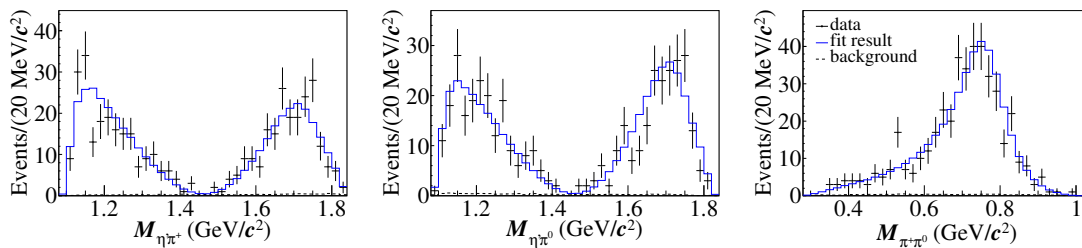

Figure 5. Projections on $M_{\eta'\pi^+}$ (left), $M_{\eta'\pi^0}$ (middle) and $M_{\pi^+\pi^0}$ (right) of the nominal fit. The data are represented by points with error bars, the fit results by the blue solid line, and the background events of signal-subtracted inclusive MC sample by the black dashed line.

Amplitude	significance (σ)
$D_s^+ \to \rho(1450)^+\eta', \rho(1450)^+ \to \pi^+\pi^0$	0.9
$D_s^+ \to a_0(1450)^+\pi^0, a_0(1450)^+ \to \pi^+\eta'$	2.4
$D_s^+ \to a_0(1450)^0\pi^+, a_0(1450)^0 \to \pi^0\eta'$	2.8
$D_s^+ \to \pi_1(1400)^+\pi^0, \pi_1(1400)^+ \to \pi^+\eta'$	0.5
$D_s^+ \to \pi_1(1400)^0\pi^+, \pi_1(1400)^0 \to \pi^0\eta'$	1.4
$D_s^+ \to \pi_1(1600)^+\pi^0, \pi_1(1600)^+ \to \pi^+\eta'$	2.7
$D_s^+ \to \pi_1(1600)^0\pi^+, \pi_1(1600)^0 \to \pi^0\eta'$	2.2
$D_s^+ \to a_2(1320)^+\pi^0, a_2(1320)^+ \to \pi^+\eta'$	0.3
$D_s^+ \to a_2(1320)^0\pi^+, a_2(1320)^0 \to \pi^0\eta'$	2.6

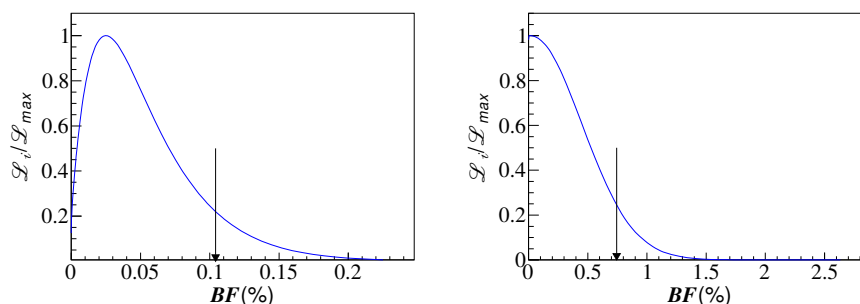**Table 4**. Tested amplitudes, but not included in the nominal fit.

Figure 6. Likelihood versus the BF of $D_s^+ \to (\pi^+\pi^0)_S \eta'$ (left) and $D_s^+ \to (\pi^+\pi^0)_P \eta'$ (right). The result obtained with incorporating the systematic uncertainty is shown in blue curve. The $\mathscr{L}_{\max}$ denotes the maximum likelihood obtained from the fit. The black arrows show the results corresponding to the 90% confidence level.

ii The ρ^+ lineshape. The uncertainties related to the lineshape of the ρ^+ are estimated by using a Breit-Wigner function instead of the Gounaris-Sakurai description.

iii R values. The radii of the nonresonant states and $D_s^\pm$ mesons are varied within the range $[2.0, 4.0]\,\text{GeV}^{-1}$ for intermediate resonances and $[4.0, 6.0]\,\text{GeV}^{-1}$ for $D_s^\pm$ mesons.

iv Background estimation. The uncertainties associated with the background estimation are studied by varying the signal fraction, i.e. w_{sig} in eq. (4.10), by its statistical uncertainty. The largest differences from the nominal results are assigned as the uncertainties. The other source of potential bias arise from the knowledge of the background distributions. An alternative MC-simulated shape is used where the relative fractions of backgrounds from $q\bar{q}$ and non-$D_s^{*\pm}D_s^{\mp}$ open charm are varied by the statistical uncertainties of their cross sections.

v Detector effects. These effects are related to the efficiency difference between MC simulation and data caused by PID and tracking, reflected in the $\gamma_\epsilon(p)$ in eq. (4.5). The uncertainties associated with $\gamma_\epsilon(p)$ are obtained by performing alternative amplitude analyses varying PID and tracking efficiencies according to their uncertainties. The systematic uncertainty from this source is found to be negligible.

The assigned systematic uncertainties on the fit fractions (FF) for the S-wave and P-wave nonresonant components are summarized in table 5. The FF for the L-wave nonresonant amplitude is defined as

$$\text{FF}_L = \frac{\sum^{N_{\text{gen}}} |\rho_L \mathcal{N}_L|^2}{\sum^{N_{\text{gen}}} |\mathcal{M}|^2}, \tag{4.21}$$

where N_{gen} is the number of phase-space MC events at generator level. It involves the phase-space MC truth information without detector acceptance or resolution effects.

Source	Systematic Uncertainty (%)	
	$D_s^+ \to (\pi^+\pi^0)_S\eta'$	$D_s^+ \to (\pi^+\pi^0)_P\eta'$
Resonance parameters	<0.1	<0.1
ρ^+ lineshape	<0.1	<0.1
R values	0.1	3.3
Background	0.2	0.1
Total	0.2	3.3

Table 5. Systematic uncertainties on FFs for S-wave and P-wave nonresonant components.

5 Branching fraction measurement

The ST D_s^- mesons are reconstructed through all twelve hadronic decays as shown in table 3 and the selection criteria are the same as those described in section 3 for the branching fraction measurement. In addition, all pions are required to have momenta greater than $100\,\mathrm{MeV}/c$ to remove soft pions from D^{*+} decays. The best tag candidate with M_{rec} closest to the $D_s^{*\pm}$ known mass [4] is chosen if there are multiple ST candidates. The data sets are organized into three sample groups, $4.178\,\mathrm{GeV}$, 4.189–$4.219\,\mathrm{GeV}$, and $4.226\,\mathrm{GeV}$, that were acquired during the same year under consistent running condition. The yields for various tag modes are obtained by fitting the corresponding M_{tag} distributions. As an example, the fits to the M_{tag} distributions of the accepted ST candidates from the data sample at $\sqrt{s} = 4.178\,\mathrm{GeV}$ are shown in figure 7. In the fits, the signal is modeled by a MC-simulated shape convolved with a Gaussian function to account for differences in resolution between data and MC simulation. The background is described by a second-order Chebyshev polynomial. Inclusive MC studies show that there is no peaking background in any tag mode, except for $D^- \to K_S^0\pi^-$ and $D_s^- \to \eta\pi^+\pi^-\pi^-$ faking the $D_s^- \to K_S^0 K^-$ and $D_s^- \to \pi^-\eta'$ tags, respectively. Therefore, the MC-simulated shapes of these two peaking background sources are added to the background polynomial functions.

Once a tag mode is reconstructed, we select the signal decay $D_s^+ \to \pi^+\pi^0\eta'$. In the case of multiple candidates, the DT candidate with the average mass, $(M_{\mathrm{sig}} + M_{\mathrm{tag}})/2$, closest to the $D_s^\pm$ nominal mass listed in the PDG [4] is retained.

To measure the BF, we employ the following equations:

$$N_{\mathrm{tag}}^{\mathrm{ST}} = 2N_{D_s^+D_s^-}\mathcal{B}_{\mathrm{tag}}\epsilon_{\mathrm{tag}}^{\mathrm{ST}}, \tag{5.1}$$

$$N_{\mathrm{tag,sig}}^{\mathrm{DT}} = 2N_{D_s^+D_s^-}\mathcal{B}_{\mathrm{tag}}\mathcal{B}_{\mathrm{sig}}\epsilon_{\mathrm{tag,sig}}^{\mathrm{DT}}, \tag{5.2}$$

where $N_{\mathrm{tag}}^{\mathrm{ST}}$ is the ST yield for the tag mode; $N_{\mathrm{tag,sig}}^{\mathrm{DT}}$ is the DT yield; $N_{D_s^+D_s^-}$ is the total number of $D_s^{*\pm}D_s^\mp$ pairs produced from the e^+e^- collisions; $\mathcal{B}_{\mathrm{tag}}$ and $\mathcal{B}_{\mathrm{sig}}$ are the BFs of the tag and signal modes, respectively; $\epsilon_{\mathrm{tag}}^{\mathrm{ST}}$ is the ST efficiency to reconstruct the tag mode; and $\epsilon_{\mathrm{tag,sig}}^{\mathrm{DT}}$ is the DT efficiency to reconstruct both the tag and the signal decay modes. In the case of more than one tag mode and sample group,

$$N_{\mathrm{total}}^{\mathrm{DT}} = \Sigma_{\alpha,i}N_{\alpha,\mathrm{sig},i}^{\mathrm{DT}} = \mathcal{B}_{\mathrm{sig}}\Sigma_{\alpha,i}2N_{D_s^+D_s^-}^i\mathcal{B}_\alpha\epsilon_{\alpha,\mathrm{sig},i}^{\mathrm{DT}}, \tag{5.3}$$
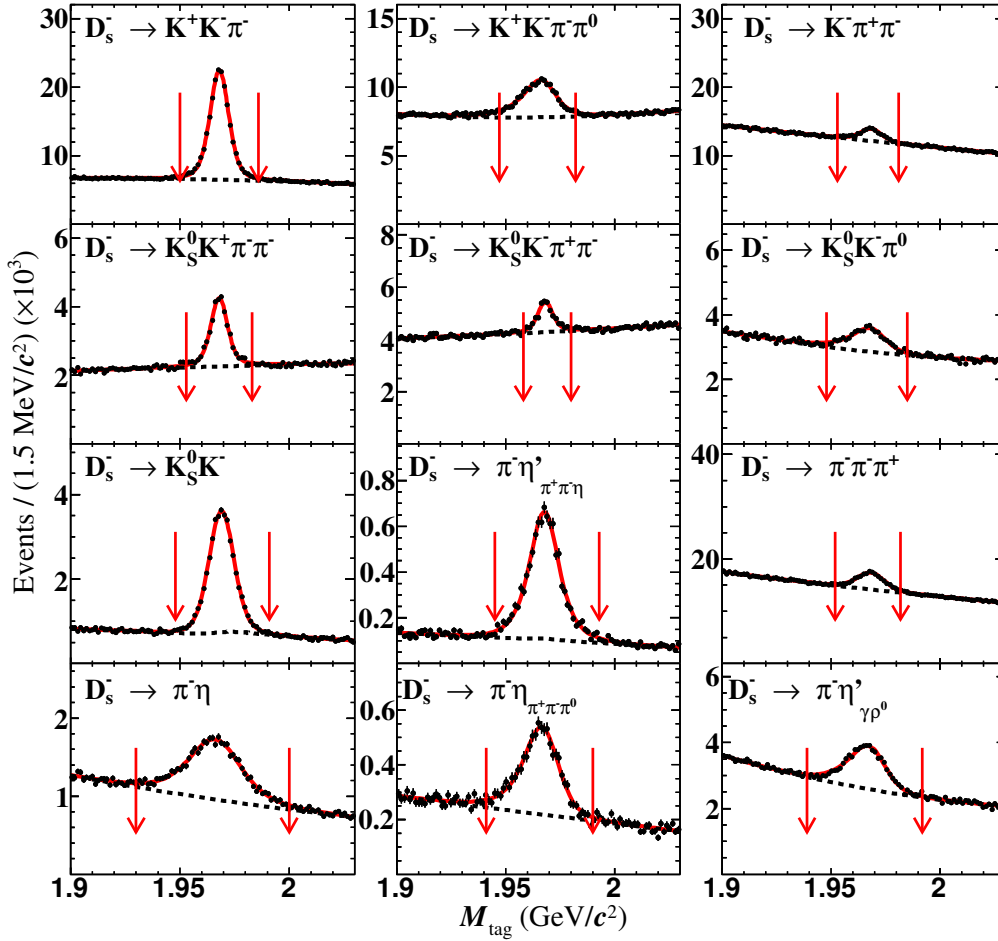
Figure 7. Fits to the M_{tag} distributions of the ST candidates from the data sample at $\sqrt{s} = 4.178\,\text{GeV}$. The points with error bars are data, the red solid lines are the total fits, and the black dashed lines are background. The pairs of red arrows denote the signal regions.

where α represents the tag mode in the ith sample group. By isolating $\mathcal{B}_{\text{sig}}$ and replacing $N_{D_s^+ D_s^-}$ shown in eq. (5.1), we find

$$\mathcal{B}_{\text{sig}} = \frac{N_{\text{fitted}}^{\text{DT}} - N_{\text{peaking}}^{\text{DT}}}{\mathcal{B}_{\eta \to \gamma\gamma} \mathcal{B}_{\pi^0 \to \gamma\gamma} \mathcal{B}_{\eta' \to \pi^+\pi^-\eta} \sum_{\alpha,i} N_{\alpha,i}^{\text{ST}} \epsilon_{\alpha,\text{sig},i}^{\text{DT}} / \epsilon_{\alpha,i}^{\text{ST}}}, \tag{5.4}$$

where $N_{\alpha,i}^{\text{ST}}$ is obtained from the data sample, while $N_{\text{peaking}}^{\text{DT}}$, $\epsilon_{\alpha,\text{sig},i}^{\text{DT}}$ and $\epsilon_{\alpha,i}^{\text{ST}}$ are obtained from the inclusive MC sample. The $D_s^+ \to \pi^+\pi^0\eta'$ simulated sample is generated according to the results of the amplitude analysis. The BFs $\mathcal{B}_{\eta \to \gamma\gamma}$, $\mathcal{B}_{\pi^0 \to \gamma\gamma}$ and $\mathcal{B}_{\eta' \to \pi^+\pi^-\eta}$ have been introduced to consider these sub-channels.

The $N_{\text{fitted}}^{\text{DT}}$ is obtained from the fit to the M_{sig} distribution of the selected $D_s^+ \to \pi^+\pi^0\eta'$ candidates. The fit result is shown in figure 8, where the signal shape is described by a MC-simulated shape convolved with a Gaussian function to account for differences in res-
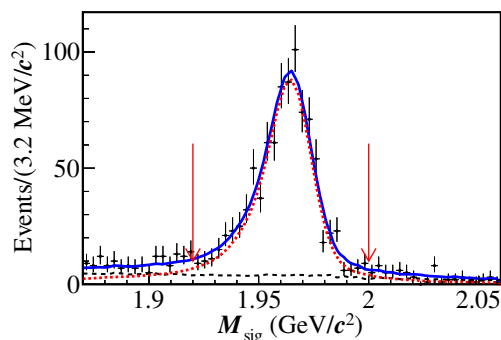
Figure 8. Fit to the $M_{\rm sig}$ distribution of the DT candidates from the data samples at $\sqrt{s} = 4.178$–4.226 GeV. This plot is obtained using twelve tag modes in table 3. The data are represented by points with error bars, the total fit by the blue solid line, and the fitted signal and the fitted background by the red dotted and the black dashed lines, respectively. The pair of red arrows indicate the signal region.

olution between data and MC. The background shape is described by a MC-simulated shape which excludes peaking background from $D_s^+ \to \pi^+ \eta \omega_{\pi^+ \pi^- \pi^0}$. The number of peaking background events, $N^{\rm DT}_{\rm peaking}$ is estimated from the inclusive MC sample. Thus, $N^{\rm DT}_{\rm fitted}$ and $N^{\rm DT}_{\rm peaking}$ are determined to be 837 ± 35 and 5 ± 1, respectively. Tables 6–8 summarize the ST efficiencies, DT efficiencies, and ST yields in data samples at the C.M. energies $\sqrt{s} = 4.178 - 4.226$ GeV. Taking into account the differences in $\pi^{\pm}$ tracking/PID efficiencies, π^0 and η reconstruction efficiencies between data and MC simulation, we determine the BF $\mathcal{B}(D_s^+ \to \pi^+ \pi^0 \eta') = (6.15 \pm 0.25({\rm stat.}) \pm 0.18({\rm syst.}))\%$ according to eq. (5.4).

The following sources of the systematic uncertainties are taken into account for the BF measurement.

- The number of ST D_s^+ mesons. The systematic uncertainty due to the total yield of the ST D_s^- mesons is assigned to be 0.9% by taking into account the background fluctuation in the fit, and examining the changes of the fit yields by using alternative signal and background shapes.

- Background shape. The systematic uncertainty due to the MC-simulated background shape is studied by varying the relative fractions of the background from $q\bar{q}$ or non-$D_s^{*+} D_s^-$ open charm by the statistical uncertainties of their related cross sections. It is found that the uncertainty arising from this source is 0.1% which is small enough to be neglected.

- π^+ tracking/PID efficiency. The tracking efficiency for π^+ mesons is studied with a $e^+ e^- \to K^+ K^- \pi^+ \pi^-$ control sample. The data-MC tracking efficiency ratios for π^+ from D_s^+ is 1.000 ± 0.003 and that for π^+ (π^-) from η' are 0.988 ± 0.008 (0.983 ± 0.008). The PID efficiency for π^+ mesons is studied with $e^+ e^- \to K^+ K^- \pi^+ \pi^- (\pi^0)$ and $e^+ e^- \to \pi^+ \pi^- \pi^+ \pi^- (\pi^0)$ control samples. The data-MC PID efficiency ratios for π^+ from D_s^+ and $\pi^{\pm}$ from η' are 0.996 ± 0.003 and 0.992 ± 0.002, respectively. Thus,

Tag mode	$N_{\rm ST}$	$\epsilon_{\rm ST}(\%)$	$\epsilon_{\rm DT}(\%)$
$D_s^- \to K_S^0 K^-$	31941 ± 312	47.36 ± 0.07	6.30 ± 0.18
$D_s^- \to K^+ K^- \pi^-$	137240 ± 614	39.47 ± 0.03	5.08 ± 0.07
$D_s^- \to K_S^0 K^- \pi^0$	11385 ± 529	16.12 ± 0.11	2.19 ± 0.10
$D_s^- \to K_S^0 K^- \pi^- \pi^+$	8093 ± 326	20.40 ± 0.12	2.06 ± 0.13
$D_s^- \to K_S^0 K^+ \pi^- \pi^-$	15719 ± 289	21.83 ± 0.06	2.50 ± 0.11
$D_s^- \to \pi^- \eta_{\gamma\gamma}$	17940 ± 402	43.58 ± 0.15	5.91 ± 0.21
$D_s^- \to \pi^- \eta'_{\pi^+\pi^-\eta_{\gamma\gamma}}$	7759 ± 141	19.12 ± 0.06	2.22 ± 0.13
$D_s^- \to K^- \pi^+ \pi^-$	17423 ± 666	47.46 ± 0.22	6.15 ± 0.21
$D_s^- \to K^- K^+ \pi^- \pi^0$	39306 ± 799	10.50 ± 0.03	1.30 ± 0.03
$D_s^- \to \pi^- \pi^- \pi^+$	37977 ± 859	51.43 ± 0.15	6.77 ± 0.17
$D_s^- \to \pi^- \eta_{\pi^+\pi^-\pi^0}$	5102 ± 172	20.85 ± 0.10	2.57 ± 0.19
$D_s^- \to \pi^- \eta'_{\gamma\rho^0}$	20580 ± 538	26.28 ± 0.10	3.79 ± 0.13

Table 6. The efficiencies and ST yields at $\sqrt{s} = 4.178\,{\rm GeV}$. The uncertainties are statistical.

Tag mode	$N_{\rm ST}$	$\epsilon_{\rm ST}(\%)$	$\epsilon_{\rm DT}(\%)$
$D_s^- \to K_S^0 K^-$	18559 ± 261	47.26 ± 0.09	6.41 ± 0.23
$D_s^- \to K^+ K^- \pi^-$	81286 ± 505	39.32 ± 0.04	5.12 ± 0.09
$D_s^- \to K_S^0 K^- \pi^0$	6832 ± 457	15.71 ± 0.16	2.28 ± 0.14
$D_s^- \to K_S^0 K^- \pi^- \pi^+$	5269 ± 282	20.19 ± 0.17	2.13 ± 0.17
$D_s^- \to K_S^0 K^+ \pi^- \pi^-$	8948 ± 231	21.63 ± 0.09	2.48 ± 0.14
$D_s^- \to \pi^- \eta_{\gamma\gamma}$	10025 ± 339	43.00 ± 0.22	6.14 ± 0.28
$D_s^- \to \pi^- \eta'_{\pi^+\pi^-\eta_{\gamma\gamma}}$	4428 ± 111	19.00 ± 0.08	2.42 ± 0.18
$D_s^- \to K^- \pi^+ \pi^-$	10175 ± 448	47.19 ± 0.32	6.22 ± 0.28
$D_s^- \to K^- K^+ \pi^- \pi^0$	23311 ± 659	10.58 ± 0.05	1.24 ± 0.04
$D_s^- \to \pi^- \pi^- \pi^+$	21909 ± 776	50.35 ± 0.22	7.03 ± 0.23
$D_s^- \to \pi^- \eta_{\pi^+\pi^-\pi^0}$	3185 ± 146	20.79 ± 0.14	2.69 ± 0.25
$D_s^- \to \pi^- \eta'_{\gamma\rho^0}$	11937 ± 480	26.09 ± 0.14	3.33 ± 0.16

Table 7. The efficiencies and ST yields at $\sqrt{s} = 4.189 - 4.219\,{\rm GeV}$. The uncertainties are statistical.

Tag mode	N_{ST}	$\epsilon_{\mathrm{ST}}(\%)$	$\epsilon_{\mathrm{DT}}(\%)$
$D_s^- \to K_S^0 K^-$	6582 ± 160	46.37 ± 0.16	6.41 ± 0.37
$D_s^- \to K^+ K^- \pi^-$	28439 ± 327	38.38 ± 0.07	5.07 ± 0.15
$D_s^- \to K_S^0 K^- \pi^0$	2227 ± 220	15.93 ± 0.29	1.89 ± 0.20
$D_s^- \to K_S^0 K^- \pi^- \pi^+$	1662 ± 217	19.50 ± 0.31	2.12 ± 0.27
$D_s^- \to K_S^0 K^+ \pi^- \pi^-$	3263 ± 172	21.29 ± 0.15	2.46 ± 0.23
$D_s^- \to \pi^- \eta_{\gamma\gamma}$	3725 ± 252	41.83 ± 0.41	6.29 ± 0.47
$D_s^- \to \pi^- \eta'_{\pi^+\pi^-\eta_{\gamma\gamma}}$	$1648 \pm\ \ 74$	18.56 ± 0.13	2.22 ± 0.28
$D_s^- \to K^- \pi^+ \pi^-$	4984 ± 458	45.66 ± 0.59	7.14 ± 0.50
$D_s^- \to K^- K^+ \pi^- \pi^0$	7785 ± 453	10.39 ± 0.09	1.39 ± 0.08
$D_s^- \to \pi^- \pi^- \pi^+$	7511 ± 393	49.32 ± 0.41	7.06 ± 0.37
$D_s^- \to \pi^- \eta_{\pi^+\pi^-\pi^0}$	$1044 \pm\ \ 78$	20.31 ± 0.25	2.63 ± 0.40
$D_s^- \to \pi^- \eta'_{\gamma\rho^0}$	3813 ± 335	25.94 ± 0.27	3.83 ± 0.28

Table 8. The efficiencies and ST yields at $\sqrt{s} = 4.226\,\mathrm{GeV}$. The uncertainties are statistical.

the systematic uncertainties associated with the total charged-particle tracking (PID) efficiency is determined to be 1.9% (0.7%).

- π^0, η reconstruction. The systematic uncertainty associated with the π^0 reconstruction efficiency is investigated by using a control sample of the process $e^+e^- \to K^+K^-\pi^+\pi^-\pi^0$. The same selection criteria described in section 3 are used to reconstruct the two kaons and the two pions. The recoiling mass distribution of $K^+K^-\pi^+\pi^-$ is fitted to obtain the total number of π^0s and the π^0 selection is applied to determine the number of reconstructed π^0 mesons. The average ratio between data and MC efficiencies of π^0 reconstruction, weighted by the corresponding momentum spectra, is estimated to be 1.006 ± 0.009. Similarly, the average ratio between data and MC efficiencies of η reconstruction is estimated to be 1.011 ± 0.010. After correcting the efficiencies, the systematic uncertainties associated with reconstruction efficiencies are 0.9% for π^0 and 1.0% for η mesons.

- MC sample size. The uncertainty arising from the finite MC sample size is obtained by $\sqrt{\sum_\alpha \left(f_\alpha \frac{\delta_{\epsilon_\alpha}}{\epsilon_\alpha} \right)^2}$, where f_α is the tag-yield fraction, and ϵ_α and δ_{ϵ_α} are the signal efficiency and the corresponding uncertainty of tag mode α, respectively.

- Amplitude model. The uncertainty from the amplitude model is estimated by varying the amplitude-model parameters. For the mass and width of ρ^+ resonance, we sample them with a Gaussian distribution in which the mean and width are set to the corresponding known value and uncertainty from PDG [4]. Meanwhile, we uniformly

Source	Uncertainty (%)
The number of ST D_s^+	0.9
Tracking	1.9
PID	0.7
π^0 reconstruction	0.9
η reconstruction	1.0
MC statistics	0.2
Amplitude model	0.4
Peaking background	0.2
BF of $\eta' \to \pi^+\pi^-\eta$	1.2
BF of $\eta \to \gamma\gamma$	0.5
Total	2.9

Table 9. Systematic uncertainties in the BF measurement.

vary the effective radii of Blatt-Weisskopf Barrier within the range $[2.0, 4.0]\,\mathrm{GeV}/c^{-1}$ for intermediate resonances and $[4.0, 6.0]\,\mathrm{GeV}/c^{-1}$ for D_s mesons. The distribution of 600 efficiencies resulting from this variation is fitted by a Gaussian function and the fitted width divided by the mean value is taken as an uncertainty.

- Peaking background. The uncertainties caused by peaking background is studied by varying the BF of $D_s^+ \to \pi^+\eta\omega_{\pi^+\pi^-\pi^0}$ from 0.85% to 1.39% based on the precision of the measured branching ratio [4]. The shift in DT yield is 0.2%, which is taken as the corresponding uncertainty.

All of the systematic uncertainties are summarized in table 9. Adding them in quadrature gives a total systematic uncertainty in the BF measurement of 2.9%.

6 Summary

This paper presents the amplitude analysis of the decay $D_s^+ \to \pi^+\pi^0\eta'$ with $6.32\,\mathrm{fb}^{-1}$ of e^+e^- collision data samples at $\sqrt{s} = 4.178 - 4.226\,\mathrm{GeV}$. The mode $D_s^+ \to \rho\eta'$ is found to be the main intermediate process contributing to this final state. In addition, we also report the upper limits of the BFs of S-wave and P-wave nonresonant components of $D_s^+ \to \pi^+\pi^0\eta'$ to be $\mathcal{B}(D_s^+ \to (\pi^+\pi^0)_S\eta') < 0.10\%$ and $\mathcal{B}(D_s^+ \to (\pi^+\pi^0)_P\eta') < 0.74\%$ at the 90% confidence level, respectively.

We also measure $\mathcal{B}(D_s^+ \to \pi^+\pi^0\eta') = (6.15 \pm 0.25 \pm 0.18)\%$ which is consistent within 1σ of the CLEO result $\mathcal{B}(D_s^+ \to \pi^+\pi^0\eta') = (5.6 \pm 0.5 \pm 0.6)\%$ but has a significantly improved precision. Furthermore, the branching fraction of the $D_s^+ \to \rho^+\eta'$ decay is $(6.15 \pm 0.25(\mathrm{stat.}) \pm 0.18(\mathrm{syst.}))\%$ based on the amplitude analysis results. This result is more than 3σ above current theoretical predictions and suggests that other contributions, such as, QCD flavor-singlet hairpin amplitude [5], should be taken into account.

Acknowledgments

References

[1] B. Bhattacharya and J.L. Rosner, *Decays of Charmed Mesons to PV Final States*, *Phys. Rev. D* **79** (2009) 034016 [*Erratum ibid.* **81** (2010) 099903] [arXiv:0812.3167] [INSPIRE].

[2] H.-Y. Cheng and C.-W. Chiang, *Two-body hadronic charmed meson decays*, *Phys. Rev. D* **81** (2010) 074021 [arXiv:1001.0987] [INSPIRE].

[3] P. Bickert and S. Scherer, *Two-photon decays and transition form factors of π^0, η, and η' in large-N_c chiral perturbation theory*, *Phys. Rev. D* **102** (2020) 074019 [arXiv:2005.08550] [INSPIRE].

[4] PARTICLE DATA collaboration, *Review of Particle Physics*, *Prog. Theor. Exp. Phys.* **2020** (2020) 083C01 [INSPIRE].

[5] H.-Y. Cheng and S. Oh, *Flavor* SU(3) *symmetry and QCD factorization in $B \to PP$ and PV decays*, *JHEP* **09** (2011) 024 [arXiv:1104.4144] [INSPIRE].

[6] H.-Y. Cheng, C.-W. Chiang and A.-L. Kuo, *Global analysis of two-body $D \to VP$ decays within the framework of flavor symmetry*, *Phys. Rev. D* **93** (2016) 114010 [arXiv:1604.03761] [INSPIRE].

[7] F.-S. Yu, X.-X. Wang and C.-D. Lu, *Nonleptonic Two Body Decays of Charmed Mesons*, *Phys. Rev. D* **84** (2011) 074019 [`arXiv:1101.4714`] [InSPIRE].

[8] Q. Qin, H.-n. Li, C.-D. Lü and F.-S. Yu, *Branching ratios and direct CP asymmetries in $D \to PV$ decays*, *Phys. Rev. D* **89** (2014) 054006 [`arXiv:1305.7021`] [InSPIRE].

[9] CLEO collaboration, *Improved Measurement of Absolute Hadronic Branching Fractions of the D_s^+ Meson*, *Phys. Rev. D* **88** (2013) 032009 [`arXiv:1306.5363`] [InSPIRE].

[10] BESIII collaboration, *Measurement of the branching fractions of $D_s^+ \to \eta' X$ and $D_s^+ \to \eta' \rho^+$ in $e^+ e^- \to D_s^+ D_s^-$*, *Phys. Lett. B* **750** (2015) 466 [`arXiv:1506.08952`] [InSPIRE].

[11] M. Ablikim et al., *Design and Construction of the BESIII Detector*, *Nucl. Instrum. Meth. A* **614** (2010) 345 [`arXiv:0911.4960`] [InSPIRE].

[12] C. Yu et al., *BEPCII Performance and Beam Dynamics Studies on Luminosity*, in proceedings of the *7th International Particle Accelerator Conference (IPAC'16)*, Busan, Korea, 8–13 May 2016, JACoW, Geneva, Switzerland (2016), pp. 1014–1018 [InSPIRE].

[13] BESIII collaboration, *Future Physics Programme of BESIII*, *Chin. Phys. C* **44** (2020) 040001 [`arXiv:1912.05983`] [InSPIRE].

[14] X. Li et al., *Study of MRPC technology for BESIII endcap-TOF upgrade*, *Radiat. Detect. Technol. Meth.* **1** (2017) 13.

[15] Y.-X. Guo et al., *The study of time calibration for upgraded end cap TOF of BESIII*, *Radiat. Detect. Technol. Meth.* **1** (2017) 15.

[16] P. Cao et al., *Design and construction of the new BESIII endcap Time-of-Flight system with MRPC technology*, *Nucl. Instrum. Meth. A* **953** (2020) 163053.

[17] BESIII collaboration, *Measurement of the integrated luminosities at BESIII for data samples at collision energies around $4\,GeV$*, submitted to Chin. Phys. C, [`arXiv:2203.03133`] [InSPIRE].

[18] CLEO collaboration, *Measurement of Charm Production Cross Sections in $e^+ e^-$ Annihilation at Energies between 3.97 and $4.26\,GeV$*, *Phys. Rev. D* **80** (2009) 072001 [`arXiv:0801.3418`] [InSPIRE].

[19] GEANT4 collaboration, *GEANT4 — a simulation toolkit*, *Nucl. Instrum. Meth. A* **506** (2003) 250 [InSPIRE].

[20] S. Jadach, B.F.L. Ward and Z. Wąs, *Coherent exclusive exponentiation for precision Monte Carlo calculations*, *Phys. Rev. D* **63** (2001) 113009 [`hep-ph/0006359`] [InSPIRE].

[21] S. Jadach, B.F.L. Ward and Z. Wąs, *The Precision Monte Carlo event generator KK for two fermion final states in $e^+ e^-$ collisions*, *Comput. Phys. Commun.* **130** (2000) 260 [`hep-ph/9912214`] [InSPIRE].

[22] D.J. Lange, *The EvtGen particle decay simulation package*, *Nucl. Instrum. Meth. A* **462** (2001) 152 [InSPIRE].

[23] R.-G. Ping, *Event generators at BESIII*, *Chin. Phys. C* **32** (2008) 599 [InSPIRE].

[24] H.-M. Hu, *Hadronic fragmentation*, *Int. J. Mod. Phys. A* **24S1** (2009) 103.

[25] B. Andersson and H.-m. Hu, *Few body states in Lund string fragmentation model*, [`hep-ph/9910285`] [InSPIRE].

[26] H.-m. Hu and A. Tai, *Production at intermediate-energies and Lund area law, eConf C* **010430** (2001) T24 [hep-ex/0106017].

[27] J.C. Chen, G.S. Huang, X.R. Qi, D.H. Zhang and Y.S. Zhu, *Event generator for J/ψ and $\psi(2S)$ decay*, *Phys. Rev. D* **62** (2000) 034003 [INSPIRE].

[28] R.-L. Yang, R.-G. Ping and H. Chen, *Tuning and Validation of the Lundcharm Model with J/ψ Decays*, *Chin. Phys. Lett.* **31** (2014) 061301 [INSPIRE].

[29] E. Richter-Was, *QED bremsstrahlung in semileptonic B and leptonic tau decays*, *Phys. Lett. B* **303** (1993) 163 [INSPIRE].

[30] MARK-III collaboration, *Direct Measurements of Charmed-D-Meson Hadronic Branching Fractions*, *Phys. Rev. Lett.* **56** (1986) 2140 [INSPIRE].

[31] W. Verkerke and D.P. Kirkby, *RooFit Users Manual v2.07*, (2006) http://roofit.sourceforge.net.

[32] BESIII collaboration, *Amplitude analysis and branching fraction measurement of $D_s^+ \to K^+K^-\pi^+$*, *Phys. Rev. D* **104** (2021) 012016 [arXiv:2011.08041] [INSPIRE].

[33] G.J. Gounaris and J.J. Sakurai, *Finite width corrections to the vector meson dominance prediction for $\rho \to e^+e^-$*, *Phys. Rev. Lett.* **21** (1968) 244 [INSPIRE].

[34] B.S. Zou and D.V. Bugg, *Covariant tensor formalism for partial wave analyses of ψ decay to mesons*, *Eur. Phys. J. A* **16** (2003) 537 [hep-ph/0211457] [INSPIRE].

The BESIII collaboration

M. Ablikim,[1] M.N. Achasov,[10,b] P. Adlarson,[67] S. Ahmed,[15] M. Albrecht,[4] R. Aliberti,[28] A. Amoroso,[66A,66C] M.R. An,[32] Q. An,[63,49] X.H. Bai,[57] Y. Bai,[48] O. Bakina,[29] R.B. Ferroli,[23A] I. Balossino,[24A] Y. Ban,[38,i] K. Begzsuren,[26] N. Berger,[28] M. Bertani,[23A] D. Bettoni,[24A] F. Bianchi,[66A,66C] J. Bloms,[60] A. Bortone,[66A,66C] I. Boyko,[29] R.A. Briere,[5] H. Cai,[68] X. Cai,[1,49] A. Calcaterra,[23A] G.F. Cao,[1,54] N. Cao,[1,54] S.A. Cetin,[53A] J.F. Chang,[1,49] W.L. Chang,[1,54] G. Chelkov,[29,a] D.Y. Chen,[6] G. Chen,[1] H.S. Chen,[1,54] M.L. Chen,[1,49] S.J. Chen,[35] X.R. Chen,[25] Y.B. Chen,[1,49] Z.J. Chen,[20,j] W.S. Cheng,[66C] G. Cibinetto,[24A] F. Cossio,[66C] X.F. Cui,[36] H.L. Dai,[1,49] X.C. Dai,[1,54] A. Dbeyssi,[15] R.E. de Boer,[4] D. Dedovich,[29] Z.Y. Deng,[1] A. Denig,[28] I. Denysenko,[29] M. Destefanis,[66A,66C] F. De Mori,[66A,66C] Y. Ding,[33] C. Dong,[36] J. Dong,[1,49] L.Y. Dong,[1,54] M.Y. Dong,[1,49,54] X. Dong,[68] S.X. Du,[71] Y.L. Fan,[68] J. Fang,[1,49] S.S. Fang,[1,54] Y. Fang,[1] R. Farinelli,[24A] L. Fava,[66B,66C] F. Feldbauer,[4] G. Felici,[23A] C.Q. Feng,[63,49] J.H. Feng,[50] M. Fritsch,[4] C.D. Fu,[1] Y. Gao,[38,i] Y. Gao,[64] Y. Gao,[63,49] Y.G. Gao,[6] I. Garzia,[24A,24B] P.T. Ge,[68] C. Geng,[50] E.M. Gersabeck,[58] A. Gilman,[61] K. Goetzen,[11] L. Gong,[33] W.X. Gong,[1,49] W. Gradl,[28] M. Greco,[66A,66C] L.M. Gu,[35] M.H. Gu,[1,49] S. Gu,[2] Y.T. Gu,[13] C.Y. Guan,[1,54] A.Q. Guo,[22] L.B. Guo,[34] R.P. Guo,[40] Y.P. Guo,[9,g] A. Guskov,[29,a] T.T. Han,[41] W.Y. Han,[32] X.Q. Hao,[16] F.A. Harris,[56] K.L. He,[1,54] F.H. Heinsius,[4] C.H. Heinz,[28] T. Held,[4] Y.K. Heng,[1,49,54] C. Herold,[51] M. Himmelreich,[11,e] T. Holtmann,[4] G.Y. Hou,[1,54] Y.R. Hou,[54] Z.L. Hou,[1] H.M. Hu,[1,54] J.F. Hu,[47,k] T. Hu,[1,49,54] Y. Hu,[1] G.S. Huang,[63,49] L.Q. Huang,[64] X.T. Huang,[41] Y.P. Huang,[1] Z. Huang,[38,i] T. Hussain,[65] N. Hüsken,[22,28] W.I. Andersson,[67] W. Imoehl,[22] M. Irshad,[63,49] S. Jaeger,[4] S. Janchiv,[26] Q. Ji,[1] Q.P. Ji,[16] X.B. Ji,[1,54] X.L. Ji,[1,49] Y.Y. Ji,[41] H.B. Jiang,[41] X.S. Jiang,[1,49,54] J.B. Jiao,[41] Z. Jiao,[18] S. Jin,[35] Y. Jin,[57] M.Q. Jing,[1,54] T. Johansson,[67] N. Kalantar-Nayestanaki,[55] X.S. Kang,[33] R. Kappert,[55] M. Kavatsyuk,[55] B.C. Ke,[71,1] I.K. Keshk,[4] A. Khoukaz,[60] P. Kiese,[28] R. Kiuchi,[1] R. Kliemt,[11] L. Koch,[30] O.B. Kolcu,[53A,d] B. Kopf,[4] M. Kuemmel,[4] M. Kuessner,[4] A. Kupsc,[67] M.G. Kurth,[1,54] W. Kühn,[30] J.J. Lane,[58] J.S. Lange,[30] P. Larin,[15] A. Lavania,[21] L. Lavezzi,[66A,66C] Z.H. Lei,[63,49] H. Leithoff,[28] M. Lellmann,[28] T. Lenz,[28] C. Li,[39] C.H. Li,[32] C. Li,[63,49] D.M. Li,[71] F. Li,[1,49] G. Li,[1] H. Li,[63,49] H. Li,[43] H.B. Li,[1,54] H.J. Li,[16] J.L. Li,[41] J.Q. Li,[4] J.S. Li,[50] K. Li,[1] L.K. Li,[1] L. Li,[3] P.R. Li,[31,l,m] S.Y. Li,[52] W.D. Li,[1,54] W.G. Li,[1] X.H. Li,[63,49] X.L. Li,[41] X. Li,[1,54] Z.Y. Li,[50] H. Liang,[63,49] H. Liang,[1,54] H. Liang,[27] Y.F. Liang,[45] Y.T. Liang,[25] G.R. Liao,[12] L.Z. Liao,[1,54] J. Libby,[21] C.X. Lin,[50] B.J. Liu,[1] C.X. Liu,[1] D. Liu,[63,49] F.H. Liu,[44] F. Liu,[1] F. Liu,[6] H.B. Liu,[13] H.M. Liu,[1,54] H. Liu,[1] H. Liu,[17] J.B. Liu,[63,49] J.L. Liu,[64] J.Y. Liu,[1,54] K. Liu,[1] K.Y. Liu,[33] L. Liu,[63,49] M.H. Liu,[9,g] P.L. Liu,[1] Q. Liu,[68] Q. Liu,[54] S.B. Liu,[63,49] S. Liu,[46] T. Liu,[1,54] W.M. Liu,[63,49] X. Liu,[31,l,m] Y. Liu,[31,l,m] Y.B. Liu,[36] Z.A. Liu,[1,49,54] Z.Q. Liu,[41] X.C. Lou,[1,49,54] F.X. Lu,[50] H.J. Lu,[18] J.D. Lu,[1,54] J.G. Lu,[1,49] X.L. Lu,[1] Y. Lu,[1] Y.P. Lu,[1,49] C.L. Luo,[34] M.X. Luo,[70] P.W. Luo,[50] T. Luo,[9,g] X.L. Luo,[1,49] X.R. Lyu,[54] F.C. Ma,[33] H.L. Ma,[1] L.L. Ma,[41] M.M. Ma,[1,54] Q.M. Ma,[1] R.Q. Ma,[1,54] R.T. Ma,[54] X.X. Ma,[1,54] X.Y. Ma,[1,49] F.E. Maas,[15] M. Maggiora,[66A,66C] S. Maldaner,[4] S. Malde,[61] Q.A. Malik,[65] A. Mangoni,[23B] Y.J. Mao,[38,i] Z.P. Mao,[1] S. Marcello,[66A,66C] Z.X. Meng,[57] J.G. Messchendorp,[55] G. Mezzadri,[24A] T.J. Min,[35] R.E. Mitchell,[22] X.H. Mo,[1,49,54] Y.J. Mo,[6] N.Y. Muchnoi,[10,b] H. Muramatsu,[59] S. Nakhoul,[11,e] Y. Nefedov,[29] F. Nerling,[11,e] I.B. Nikolaev,[10,b] Z. Ning,[1,49] S. Nisar,[8,h] S.L. Olsen,[54] Q. Ouyang,[1,49,54] S. Pacetti,[23B,23C] X. Pan,[9,g] Y. Pan,[58] A. Pathak,[1] A. Pathak,[27] P. Patteri,[23A] M. Pelizaeus,[4] H.P. Peng,[63,49] K. Peters,[11,e] J. Pettersson,[67] J.L. Ping,[34] R.G. Ping,[1,54] R. Poling,[59] V. Prasad,[63,49] H. Qi,[63,49] H.R. Qi,[52] K.H. Qi,[25] M. Qi,[35] T.Y. Qi,[9] S. Qian,[1,49] W.B. Qian,[54] Z. Qian,[50] C.F. Qiao,[54] L.Q. Qin,[12] X.P. Qin,[9]

X.S. Qin,[41] Z.H. Qin,[1,49] J.F. Qiu,[1] S.Q. Qu,[36] K.H. Rashid,[65] K. Ravindran,[21]
C.F. Redmer,[28] A. Rivetti,[66C] V. Rodin,[55] M. Rolo,[66C] G. Rong,[1,54] C. Rosner,[15]
M. Rump,[60] H.S. Sang,[63] A. Sarantsev,[29,c] Y. Schelhaas,[28] C. Schnier,[4] K. Schoenning,[67]
M. Scodeggio,[24A,24B] D.C. Shan,[46] W. Shan,[19] X.Y. Shan,[63,49] J.F. Shangguan,[46]
M. Shao,[63,49] C.P. Shen,[9] H.F. Shen,[1,54] P.X. Shen,[36] X.Y. Shen,[1,54] H.C. Shi,[63,49]
R.S. Shi,[1,54] X. Shi,[1,49] X.D. Shi,[63,49] J.J. Song,[41] W.M. Song,[27,1] Y.X. Song,[38,i]
S. Sosio,[66A,66C] S. Spataro,[66A,66C] K.X. Su,[68] P.P. Su,[46] F.F. Sui,[41] G.X. Sun,[1] H.K. Sun,[1]
J.F. Sun,[16] L. Sun,[68] S.S. Sun,[1,54] T. Sun,[1,54] W.Y. Sun,[34] W.Y. Sun,[27] X. Sun,[20,j]
Y.J. Sun,[63,49] Y.K. Sun,[63,49] Y.Z. Sun,[1] Z.T. Sun,[1] Y.H. Tan,[68] Y.X. Tan,[63,49] C.J. Tang,[45]
G.Y. Tang,[1] J. Tang,[50] J.X. Teng,[63,49] V. Thoren,[67] W.H. Tian,[43] Y.T. Tian,[25] I. Uman,[53B]
B. Wang,[1] C.W. Wang,[35] D.Y. Wang,[38,i] H.J. Wang,[31,l,m] H.P. Wang,[1,54] K. Wang,[1,49]
L.L. Wang,[1] M. Wang,[41] M.Z. Wang,[38,i] M. Wang,[1,54] W. Wang,[50] W.H. Wang,[68]
W.P. Wang,[63,49] X. Wang,[38,i] X.F. Wang,[31,l,m] X.L. Wang,[9,g] Y. Wang,[50] Y. Wang,[63,49]
Y.D. Wang,[37] Y.F. Wang,[1,49,54] Y.Q. Wang,[1] Y.Y. Wang,[31,l,m] Z. Wang,[1,49] Z.Y. Wang,[1]
Z. Wang,[54] Z. Wang,[1,54] D.H. Wei,[12] F. Weidner,[60] S.P. Wen,[1] D.J. White,[58] U. Wiedner,[4]
G. Wilkinson,[61] M. Wolke,[67] L. Wollenberg,[4] J.F. Wu,[1,54] L.H. Wu,[1] L.J. Wu,[1,54] X. Wu,[9,g]
Z. Wu,[1,49] L. Xia,[63,49] H. Xiao,[9,g] S.Y. Xiao,[1] Z.J. Xiao,[34] X.H. Xie,[38,i] Y.G. Xie,[1,49]
Y.H. Xie,[6] T.Y. Xing,[1,54] G.F. Xu,[1] Q.J. Xu,[14] W. Xu,[1,54] X.P. Xu,[46] Y.C. Xu,[54] F. Yan,[9,g]
L. Yan,[9,g] W.B. Yan,[63,49] W.C. Yan,[71] X. Yan,[46] H.J. Yang,[42,f] H.X. Yang,[1] L. Yang,[43]
S.L. Yang,[54] Y.X. Yang,[12] Y. Yang,[1,54] Z. Yang,[25] M. Ye,[1,49] M.H. Ye,[7] J.H. Yin,[1]
Z.Y. You,[50] B.X. Yu,[1,49,54] C.X. Yu,[36] G. Yu,[1,54] J.S. Yu,[20,j] T. Yu,[64] C.Z. Yuan,[1,54]
L. Yuan,[2] X.Q. Yuan,[38,i] Y. Yuan,[1] Z.Y. Yuan,[50] C.X. Yue,[32] A.A. Zafar,[65] X.Z. Zeng,[6]
Y. Zeng,[20,j] A.Q. Zhang,[1] B.X. Zhang,[1] G. Zhang,[16] H. Zhang,[63] H.H. Zhang,[27]
H.H. Zhang,[50] H.Y. Zhang,[1,49] J.J. Zhang,[43] J.L. Zhang,[69] J.Q. Zhang,[34] J.W. Zhang,[1,49,54]
J.Y. Zhang,[1] J.Z. Zhang,[1,54] J. Zhang,[1,54] J. Zhang,[1,54] L.M. Zhang,[52] L.Q. Zhang,[50]
L. Zhang,[35] S. Zhang,[50] S.F. Zhang,[35] S. Zhang,[20,j] X.D. Zhang,[37] X.Y. Zhang,[41] Y. Zhang,[61]
Y.T. Zhang,[71] Y.H. Zhang,[1,49] Y. Zhang,[63,49] Y. Zhang,[1] Z.H. Zhang,[6] Z.Y. Zhang,[68]
G. Zhao,[1] J. Zhao,[32] J.Y. Zhao,[1,54] J.Z. Zhao,[1,49] L. Zhao,[63,49] L. Zhao,[1] M.G. Zhao,[36]
Q. Zhao,[1] S.J. Zhao,[71] Y.B. Zhao,[1,49] Y.X. Zhao,[25] Z.G. Zhao,[63,49] A. Zhemchugov,[29,a]
B. Zheng,[64] J.P. Zheng,[1,49] Y. Zheng,[38,i] Y.H. Zheng,[54] B. Zhong,[34] C. Zhong,[64]
L.P. Zhou,[1,54] Q. Zhou,[1,54] X. Zhou,[68] X.K. Zhou,[54] X.R. Zhou,[63,49] X.Y. Zhou,[32]
A.N. Zhu,[1,54] J. Zhu,[36] K. Zhu,[1] K.J. Zhu,[1,49,54] S.H. Zhu,[62] T.J. Zhu,[69] W.J. Zhu,[9,g]
W.J. Zhu,[36] X.Y. Zhu,[16] Y.C. Zhu,[63,49] Z.A. Zhu,[1,54] B.S. Zou,[1] J.H. Zou[1]

1   *Institute of High Energy Physics, Beijing 100049, People's Republic of China*
2   *Beihang University, Beijing 100191, People's Republic of China*
3   *Beijing Institute of Petrochemical Technology, Beijing 102617, People's Republic of China*
4   *Bochum Ruhr-University, Bochum D-44780, Germany*
5   *Carnegie Mellon University, Pittsburgh, Pennsylvania 15213, U.S.A.*
6   *Central China Normal University, Wuhan 430079, People's Republic of China*
7   *China Center of Advanced Science and Technology, Beijing 100190, People's Republic of China*
8   *COMSATS University Islamabad, Lahore Campus, Defence Road, Off Raiwind Road, Lahore 54000, Pakistan*
9   *Fudan University, Shanghai 200443, People's Republic of China*
10 *G.I. Budker Institute of Nuclear Physics SB RAS (BINP), Novosibirsk 630090, Russia*
11 *GSI Helmholtzcentre for Heavy Ion Research GmbH, Darmstadt D-64291, Germany*
12 *Guangxi Normal University, Guilin 541004, People's Republic of China*
13 *Guangxi University, Nanning 530004, People's Republic of China*
14 *Hangzhou Normal University, Hangzhou 310036, People's Republic of China*

15 *Helmholtz Institute Mainz, Staudinger Weg 18, Mainz D-55099, Germany*

16 *Henan Normal University, Xinxiang 453007, People's Republic of China*

17 *Henan University of Science and Technology, Luoyang 471003, People's Republic of China*

18 *Huangshan College, Huangshan 245000, People's Republic of China*

19 *Hunan Normal University, Changsha 410081, People's Republic of China*

20 *Hunan University, Changsha 410082, People's Republic of China*

21 *Indian Institute of Technology Madras, Chennai 600036, India*

22 *Indiana University, Bloomington, Indiana 47405, U.S.A.*

23 *INFN Laboratori Nazionali di Frascati, (A)INFN Laboratori Nazionali di Frascati, Frascati I-00044, Italy; (B)INFN Sezione di Perugia, Perugia I-06100, Italy; (C)University of Perugia, Perugia I-06100, Italy*

24 *INFN Sezione di Ferrara, (A)INFN Sezione di Ferrara, Ferrara I-44122, Italy; (B)University of Ferrara, Ferrara I-44122, Italy*

25 *Institute of Modern Physics, Lanzhou 730000, People's Republic of China*

26 *Institute of Physics and Technology, Peace Ave. 54B, Ulaanbaatar 13330, Mongolia*

27 *Jilin University, Changchun 130012, People's Republic of China*

28 *Johannes Gutenberg University of Mainz, Johann-Joachim-Becher-Weg 45, Mainz D-55099, Germany*

29 *Joint Institute for Nuclear Research, Dubna 141980, Moscow Region, Russia*

30 *Justus-Liebig-Universitaet Giessen, II. Physikalisches Institut, Heinrich-Buff-Ring 16, Giessen D-35392, Germany*

31 *Lanzhou University, Lanzhou 730000, People's Republic of China*

32 *Liaoning Normal University, Dalian 116029, People's Republic of China*

33 *Liaoning University, Shenyang 110036, People's Republic of China*

34 *Nanjing Normal University, Nanjing 210023, People's Republic of China*

35 *Nanjing University, Nanjing 210093, People's Republic of China*

36 *Nankai University, Tianjin 300071, People's Republic of China*

37 *North China Electric Power University, Beijing 102206, People's Republic of China*

38 *Peking University, Beijing 100871, People's Republic of China*

39 *Qufu Normal University, Qufu 273165, People's Republic of China*

40 *Shandong Normal University, Jinan 250014, People's Republic of China*

41 *Shandong University, Jinan 250100, People's Republic of China*

42 *Shanghai Jiao Tong University, Shanghai 200240, People's Republic of China*

43 *Shanxi Normal University, Linfen 041004, People's Republic of China*

44 *Shanxi University, Taiyuan 030006, People's Republic of China*

45 *Sichuan University, Chengdu 610064, People's Republic of China*

46 *Soochow University, Suzhou 215006, People's Republic of China*

47 *South China Normal University, Guangzhou 510006, People's Republic of China*

48 *Southeast University, Nanjing 211100, People's Republic of China*

49 *State Key Laboratory of Particle Detection and Electronics, Beijing 100049, Hefei 230026, People's Republic of China*

50 *Sun Yat-Sen University, Guangzhou 510275, People's Republic of China*

51 *Suranaree University of Technology, University Avenue 111, Nakhon Ratchasima 30000, Thailand*

52 *Tsinghua University, Beijing 100084, People's Republic of China*

53 *Turkish Accelerator Center Particle Factory Group, (A)Istanbul Bilgi University, HEP Res. Cent., Eyup 34060, Istanbul, Turkey; (B)Near East University, Nicosia, North Cyprus, Mersin 10, Turkey*

54 *University of Chinese Academy of Sciences, Beijing 100049, People's Republic of China*

55 *University of Groningen, NL-9747 AA Groningen, The Netherlands*

56 *University of Hawaii, Honolulu, Hawaii 96822, U.S.A.*

57 *University of Jinan, Jinan 250022, People's Republic of China*

58 *University of Manchester, Oxford Road, Manchester M13 9PL, U.K.*

59 *University of Minnesota, Minneapolis, Minnesota 55455, U.S.A.*

60   *University of Muenster, Wilhelm-Klemm-Str. 9, Muenster 48149, Germany*

61   *University of Oxford, Keble Rd, Oxford, U.K. OX13RH*

62   *University of Science and Technology Liaoning, Anshan 114051, People's Republic of China*

63   *University of Science and Technology of China, Hefei 230026, People's Republic of China*

64   *University of South China, Hengyang 421001, People's Republic of China*

65   *University of the Punjab, Lahore-54590, Pakistan*

66   *University of Turin and INFN, (A) University of Turin, Turin I-10125, Italy; (B) University of Eastern Piedmont, Alessandria I-15121, Italy; (C) INFN, Turin I-10125, Italy*

67   *Uppsala University, Box 516, Uppsala SE-75120, Sweden*

68   *Wuhan University, Wuhan 430072, People's Republic of China*

69   *Xinyang Normal University, Xinyang 464000, People's Republic of China*

70   *Zhejiang University, Hangzhou 310027, People's Republic of China*

71   *Zhengzhou University, Zhengzhou 450001, People's Republic of China*

[a]   *Also at the Moscow Institute of Physics and Technology, Moscow 141700, Russia*

[b]   *Also at the Novosibirsk State University, Novosibirsk 630090, Russia*

[c]   *Also at the NRC "Kurchatov Institute", PNPI, Gatchina 188300, Russia*

[d]   *Currently at Istanbul Arel University, Istanbul 34295, Turkey*

[e]   *Also at Goethe University Frankfurt, 60323 Frankfurt am Main, Germany*

[f]   *Also at Key Laboratory for Particle Physics, Astrophysics and Cosmology, Ministry of Education; Shanghai Key Laboratory for Particle Physics and Cosmology; Institute of Nuclear and Particle Physics, Shanghai 200240, People's Republic of China*

[g]   *Also at Key Laboratory of Nuclear Physics and Ion-beam Application (MOE) and Institute of Modern Physics, Fudan University, Shanghai 200443, People's Republic of China*

[h]   *Also at Harvard University, Department of Physics, Cambridge, MA 02138, U.S.A.*

[i]   *Also at State Key Laboratory of Nuclear Physics and Technology, Peking University, Beijing 100871, People's Republic of China*

[j]   *Also at School of Physics and Electronics, Hunan University, Changsha 410082, China*

[k]   *Also at Guangdong Provincial Key Laboratory of Nuclear Science, Institute of Quantum Matter, South China Normal University, Guangzhou 510006, China*

[l]   *Also at Frontiers Science Center for Rare Isotopes, Lanzhou University, Lanzhou 730000, People's Republic of China*

[m]   *Also at Lanzhou Center for Theoretical Physics, Lanzhou University, Lanzhou 730000, People's Republic of China*